

Heat Capacity Effects Associated with the Hydrophobic Hydration and Interaction of Simple Solutes: A Detailed Structural and Energetical Analysis Based on MD Simulations

Dietmar Paschek*

Department of Physical Chemistry, Otto-Hahn Str. 6,
University of Dortmund, D-44221 Dortmund, Germany

(Dated: February 2, 2008)

We examine the SPCE and TIP5P water models using a temperature series of MD simulations in order to study heat capacity effects associated with the hydrophobic hydration and interaction of Xenon particles. The temperature interval between 275 K and 375 K along the 0.1 MPa isobar is studied. For all investigated models and state points we calculate the excess chemical potential for Xenon employing the Widom particle insertion technique. The solvation enthalpy and excess heat capacity is obtained from the temperature dependence of the chemical potentials and, alternatively, directly by Ewald summation, as well as a reaction field based method. All three different approaches provide consistent results. In addition, the employed reaction field method allows a separation of the individual components to the solvation enthalpy into solute/solvent and solvent/solvent parts. We find that the solvent/solvent contribution to the excess heat capacity is the dominating contribution, being about one order of magnitude larger than the solute/solvent part. The latter contribution is found to be due to the enlarged heat capacity of the water molecules in the hydration shell. A detailed spacial analysis of the heat capacity of the water molecules around a pair of Xenon particles at different separations reveals that the particularly enhanced heat capacity of the water molecules in the bisector plane between two Xenon atoms is responsible for the maximum of the heat capacity observed at the desolvation barrier, recently reported by Shimizu and Chan (*J. Am. Chem. Soc.*, **123**, 2083–2084 (2001)). The about 60% enlarged heat capacity of water in the concave part of the joint Xenon-Xenon hydration shell is found to be the result of a counterplay of strengthened hydrogen bonds and an enhanced breaking of hydrogen bonds with increasing temperature. Differences between the two models concerning the heat capacity in the Xenon-Xenon contact state are attributed to the different water model bulk heat capacities, and to the different spacial extension of the structure effect introduced by the hydrophobic particles. Similarities between the different states of water in the joint Xenon-Xenon hydration shell and the properties of stretched water are discussed.

I. INTRODUCTION

Nonpolar simple solutes, such as noble gases or methane, don't like to be dissolved in water: They are hydrophobic. Hence the corresponding solvation free energy is found to be large and positive [1, 2, 3]. However, the temperature dependence of the hydration free energy of hydrophobic solutes reveals a *negative* solvation enthalpy, which is counterbalanced by an also *negative* solvation entropy [1, 2, 3]. For the case of the simple solutes the latter observation has to be attributed to structural organization processes in the solvent phase, due to the lack of the solutes internal degrees of freedom. In addition, the solvation excess heat capacity is found to be *positive*, typically being in the range between $150 \text{ J K}^{-1} \text{ mol}^{-1}$ and $300 \text{ J K}^{-1} \text{ mol}^{-1}$ around 300 K [3], strongly suggesting an enhanced heat capacity of the hydration shell water. This essential feature has been used as a key ingredient to model hydrophobic hydration effects on the basis of a solvent structural (basically “hydrogen bond”) reorganization [4, 5, 6, 7].

As a consequence of overlapping hydration shells and the release of *shell* water molecules into the *bulk* phase,

the association of hydrophobic particles is found to be strengthened with increasing temperature in order to minimize the solvation entropy penalty [8, 9]. This sort of entropy-driven association process is usually referred to as *hydrophobic interaction* and has been qualitatively confirmed by numerous simulation studies [8, 9, 10, 11, 12, 13, 14, 15, 16, 17, 18, 19, 20, 21, 22, 23, 24, 25, 26, 27, 28, 29, 30]. In line with the negative net entropy of association, also a negative heat capacity contribution is expected and has been incorporated into models describing the hydrophobic association on the basis of the solvent exposed surface area [31, 32]. For a full depth review on the present status of conceptual understanding of hydrophobic effects we would like to refer to the recent review articles of Southall et al. [3], Pratt [33], and Widom [34]. In addition, Smith and Haymet [35] provide a tutorial overview over related simulation techniques.

However, recent publications by Shimizu and Chan [23, 25, 26], Rick [30] and Paschek [36] indicate that the heat capacity change, related to the association of two hydrophobic particles, exhibits a maximum located at distance of the desolvation barrier around $5.5 - 6.5 \text{ \AA}$. The presence and observed strength of the maximum has not been considered in models of the hydrophobic interaction based on the solvent accessible surface [25, 26] and has also consequences for the heat net capacity change at the contact state. Nevertheless, some uncertainty exists

*Electronic address: dietmar.paschek@udo.edu

about the strength of this effect for hydrophobic particles in the contact state. Shimizu et al. find an almost vanishing [25] contribution to the heat capacity (nearly identical heat capacities for the contact state and the fully separated state), whereas Rick [30] observes a negative net heat capacity for the associated state, being qualitatively in accord with model predictions based on the change of the solvent accessible surface. Both results were obtained for a pair of methane particles dissolved in TIP4P model water. Paschek [36] finds evidence for both scenarios, depending on the water model which is taken into account: For the case of the association of Xenon particles the SPCE model shows the behavior reported by Shimizu et al., whereas the TIP5P model corresponds to Rick’s scenario.

In this paper we will provide a quantitative energetical and structural study on the origin of the observed heat capacity effects. We would like to show that (at least for the studied model systems) the solvation heat capacity is dominated by the solvent restructuring effects and is related to the enhanced breaking of hydrogen bonds in different parts of the hydration shell with increasing temperature. In addition, we try to elaborate the reason for the observed differences between the SPCE and TIP5P models. Finally, we would like show that observed heat capacity effects can be understood from the properties of *stretched* water.

II. METHODS

A. MD Simulation details

We employ molecular dynamics (MD) simulations in the NPT ensemble using the Nosé-Hoover thermostat [37, 38] and the Rahman-Parrinello barostat [39, 40] with coupling times $\tau_T = 1.5$ ps and $\tau_p = 2.5$ ps (assuming the isothermal compressibility to be $\chi_T = 4.5 \cdot 10^{-5} \text{ bar}^{-1}$), respectively. The electrostatic interactions are treated in the “full potential” approach by the smooth particle mesh Ewald summation [41] with a real space cutoff of 0.9 nm and a mesh spacing of approximately 0.12 nm and 4th order interpolation. The Ewald convergence factor α was set to 3.38 nm^{-1} (corresponding to a relative accuracy of the Ewald sum of 10^{-5}). A 2.0 fs timestep was used for all simulations and the constraints were solved using the SETTLE procedure [42]. All simulations reported here were carried out using the GROMACS 3.1 program [43, 44]. Statistical errors in the analysis were computed using the method of Flyvbjerg and Petersen [45]. For all reported systems and different statepoints initial equilibration runs of 1 ns length were performed using the Berendsen weak coupling scheme for pressure and temperature control ($\tau_T = \tau_p = 0.5$ ps) [46].

In order to obtain the solvation enthalpies and excess heat capacities of Xenon, we follow two distinct approaches: 1) Indirectly from the temperature dependence the excess chemical potential. 2) Directly from

the energies obtained from the simulation runs. Since this procedure is just intended to show the applicability of our approach, it is applied only to the SPCE model. For this purpose we performed a series of simulations containing 500 water molecules employing the SPCE model [47] as well as a series containing 500 SPCE molecules plus an additional Xenon (Xenon-Xenon parameters: $\sigma = 3.975 \text{ \AA}$, $\epsilon k_B^{-1} = 214.7 \text{ K}$ [48]) particle. The systems were simulated at five different temperatures 275 K, 300 K, 325 K, 350 K and 375 K at a pressure of 0.1 MPa. Each of these simulations extended to 20 ns and 2×10^4 configurations were stored for further analysis.

To determine the heat capacity change for the association of Xenon particles we use MD simulations containing 500 water SPCE and TIP5P [49] molecules and 8 Xenon particles employing the simulation conditions outlined above. Again, each of the model systems is studied at 275 K, 300 K, 325 K, 350 K and 375 K at a pressure of 0.1 MPa. Here, runs over 60 ns were conducted, while storing 7.5×10^4 configurations for further analysis. The water/Xenon parameters were obtained applying the standard Lorentz-Berthelot mixing rules according to $\sigma_{ij} = (\sigma_{ii} + \sigma_{jj})/2$ and $\epsilon_{ij} = \sqrt{\epsilon_{ii}\epsilon_{jj}}$.

B. Hydrophobic Hydration and Interaction

We calculate the excess chemical potential of Xenon in water *a posteriori* from simulation trajectories obtained at constant pressure/temperature (NPT-Ensemble) conditions. For this purpose we employ the Widom particle insertion method [50, 51] according to

$$\mu_{ex} = -\beta^{-1} \ln \frac{\langle V \int d\vec{s}_{N+1} \exp(-\beta \Delta U) \rangle}{\langle V \rangle} \quad (1)$$

where $\Delta U = U(\vec{s}^{N+1}; L) - U(\vec{s}^N; L)$ is the potential energy of a randomly inserted solute ($N+1$)-particle into a configuration containing N solvent molecules. The $\vec{s}_i = L^{-1}\vec{r}_i$ (with $L = V^{1/3}$ being the length of a hypothetical cubic box) are the scaled coordinates of the particle positions and $\int d\vec{s}_{N+1}$ denotes an integration over the whole space. The brackets $\langle \dots \rangle$ indicate isothermal-isobaric averaging over the configuration space of the N -particle system (the solvent). The entropic and enthalpic contributions to the excess chemical potential can be obtained straightforwardly as temperature derivative according to

$$s_{ex} = - \left(\frac{\partial \mu_{ex}}{\partial T} \right)_P \quad \text{and} \quad h_{ex} = \mu_{ex} + T s_{ex} \quad (2)$$

and the isobaric heat capacity contribution according to

$$c_{P,ex} = -T \left(\frac{\partial^2 \mu_{ex}}{\partial T^2} \right)_P = \left(\frac{\partial h_{ex}}{\partial T} \right)_P. \quad (3)$$

In order to perform the calculation most efficiently we have made use of the excluded volume map (EVM) technique [52, 53] by mapping the occupied volume onto

a grid of approximately 0.2 \AA mesh-width. Distances smaller than $0.7 \times \sigma_{ij}$ with respect to any solute molecule (oxygen site) were neglected and the term $\exp(-\beta \Delta U)$ taken to be zero. With this setup the systematic error was estimated to be less than 0.02 kJ mol^{-1} . Although the construction of the excluded volume list needs a little additional computational effort, this simple scheme improves the efficiency of the sampling by almost two orders of magnitude. For the calculation of the Lennard-Jones insertion energies ΔU we have used cut-off distances of 9 \AA in combination with a proper cut-off correction. Each configuration has been probed by 10^3 *successful* insertions (i.e. insertions into the free volume, contributing non-vanishing Boltzmann-factors).

We use simulations containing 500 Water molecules and 8 Xenon particles to study the temperature dependence of the association behavior of Xenon. The hydrophobic interaction between the dissolved Xenon particles is quantified in terms the profile of free energy (PMF) for the association of two Xenon particles. The $w(r)$ is obtained by inverting the Xenon-Xenon radial distribution functions $g(r)$ according to

$$w(r) = -kT \ln g(r) . \quad (4)$$

We use temperature derivatives of quadratic fits of $w(r, T)$ to calculate the enthalpic and entropic contributions at each Xenon-Xenon separation r . All five temperatures 275 K, 300 K, 325 K, 350 K and 375 K were taken into account for the fits. The entropy and enthalpy contributions are then obtained as

$$s(r) = - \left(\frac{\partial w(r, T)}{\partial T} \right)_P \quad (5)$$

and

$$h(r) = w(r) + Ts(r) . \quad (6)$$

In addition, the corresponding heat capacity change relative to the bulk liquid is available according to

$$c_P(r) = -T \left(\frac{\partial^2 w(r, T)}{\partial^2 T} \right)_P . \quad (7)$$

C. “Calorimetric” Analysis

In order to provide a spacial resolution of the water contribution to the solvation excess heat capacity, we first calculate the individual potential energies of the water and solute molecules. This is done by a reaction field method based on the minimum image convention in combination with a minimum image “cubic” cutoff. This approach has been originally proposed by Neumann [54] and was discussed by Roberts and Schnitker [55, 56]. The reaction field approach in general is well suited for our purposes since it makes it easy to cleanly according the potential energy contributions to individual molecules.

For convenience we divide the potential energies in contributions assigned to the individual molecules with

$$E = \sum_{i=1}^M E_i$$

$$E_i = \left(\frac{1}{2} \sum_{j=1}^M E_{ij} \right) + E_{i,corr} , \quad (8)$$

where E_i is the potential energy assigned to molecule i , M is the total number of molecules. The molecule-molecule pair energy

$$E_{ij} = \sum_{\alpha} \sum_{\beta} 4 \epsilon_{i\alpha j\beta} \left[\left(\frac{\sigma_{i\alpha j\beta}}{r_{i\alpha j\beta}} \right)^{12} - \left(\frac{\sigma_{i\alpha j\beta}}{r_{i\alpha j\beta}} \right)^6 \right] + \frac{q_{i\alpha} q_{j\beta}}{r_{i\alpha j\beta}} \quad (9)$$

is then obtained as sum over discrete interaction sites α and β , with $r_{i\alpha j\beta} = |\vec{r}_{j\beta} - \vec{r}_{i\alpha}|$ based on the molecule/molecule center of mass minimum image separation. We employ long range corrections $E_{i,corr} = E_{i,corr}^{el} + E_{i,corr}^{LJ}$ accounting for electrostatic, as well as Lennard Jones interactions. The electrostatic correction

$$E_{i,corr}^{el} = \frac{2\pi}{3V} \vec{D} \vec{d}_i \quad (10)$$

is a reaction field term, corresponding to the cubic cutoff, assuming an infinitely large dielectric dielectric constant. Here $\vec{d}_i = \sum_{\alpha} q_{i\alpha} \vec{r}_{i\alpha}$ is the dipole moment of molecule i , $\vec{D} = \sum_i \vec{d}_i$ is the total dipole moment of all molecules in the simulation cell and V is the instantaneous volume of the simulation box. $E_{i,corr}^{el}$ has also been considered as the *extrinsic* potential and has been shown to provide configurational energies quite close to the values obtained by Ewald summation (with tin-foil boundary conditions) [55]. In order to be consistent with applied cubic cutoff procedure for the electrostatic interactions, we also use a Lennard Jones correction term for the cubic cutoff

$$E_{i,corr}^{LJ} = \frac{2}{V} \sum_{\alpha} \sum_j \sum_{\beta} \frac{\kappa_6}{b^3} (-\epsilon_{i\alpha j\beta} \sigma_{i\alpha j\beta}^6) + \frac{\kappa_{12}}{b^9} (\epsilon_{i\alpha j\beta} \sigma_{i\alpha j\beta}^{12}) , \quad (11)$$

with $b = V^{1/3}/2$ denoting the half box length. $\kappa_6 = [2 + 15\sqrt{2} \arctan(1/\sqrt{2})]/6 \approx 2.5093827$ and $\kappa_{12} = [17774 + 77409\sqrt{2} \arctan(1/\sqrt{2})]/207360 \approx 0.4106497$ are analytically integrated factors accounting for the cubic cutoff geometry. In case of the more common spherical cutoff, one would have to replace κ_6/b^3 by $4\pi/3R_c^3$ and κ_{12}/b^9 by $4\pi/9R_c^9$, with R_c being the cutoff-radius.

In addition to the procedure outlined section II B, we can as well directly use the individual energies to calculate the the solvation enthalpies and heat capacities according to

$$h_{ex} = \langle E_{\text{solute}} \rangle + \langle n_{\text{shell}} \rangle \times (\langle E_{\text{shell}} \rangle - \langle E_{\text{bulk}} \rangle) \quad (12)$$

where $\langle E_{\text{solute}} \rangle$ is the average potential energy of the solute molecule, $\langle E_{\text{shell}} \rangle$ is the average potential energy of the water molecules in a sufficiently large solvation sphere (here we use a radius of 1.0 nm) around the solute molecule, whereas $\langle E_{\text{bulk}} \rangle$ is the energy of the water molecules outside this sphere. $\langle n_{\text{shell}} \rangle$ is the corresponding number of water molecules in the solvation sphere. From the temperature dependence of h_{ex} we can obtain the corresponding heat capacities straightforwardly.

III. DISCUSSION

A. Hydrophobic Hydration

The hydration free energies μ_{ex} for Xenon, given in Table I, were obtained for a system of 500 SPCE molecules employing the Widom particle insertion method. In Figure 1 these data are shown, as well as a quadratic fit of the data with respect to the temperature. The corresponding solvation entropies and enthalpies are derived from the fitted temperature dependence, and are depicted as dotted and dashed lines in Figure 1, respectively. A detailed comparison of the thermodynamic solvation properties of Xenon and other noble gases using different water models, with experimental data, however, has been the subject of a previous publication [36]. In this contribution we would like to focus on the energetical and structural details regarding the hydration and association of hydrophobic Xenon particles.

In addition to the indirect determination of the solvation enthalpy based on the temperature dependence of the solvation free energy, also a direct calculation is possible. Therefore we have to consider the potential energy of the solute molecule, as well as the change of the energy of the water molecules in the solvation sphere relative to the bulk. Another *brute force* approach according to Durell and Wallqvist [57], however, is to determine the energy difference between simulations of two distinct systems, one containing only the solvent water, and another, consisting of water plus an additional solute molecule. This procedure has also been applied to the case of Xenon and

| T/K | $\mu_{ex}/\text{kJ mol}^{-1}$ |
|-------|-------------------------------|
| 275 | 6.15 ± 0.1 |
| 300 | 7.71 ± 0.1 |
| 325 | 9.05 ± 0.1 |
| 350 | 9.87 ± 0.1 |
| 375 | 10.41 ± 0.1 |

TABLE I: Calculated excess chemical potential μ_{ex} for Xenon dissolved in SPCE water, obtained from the 500 molecule systems by the Widom particle insertion technique.

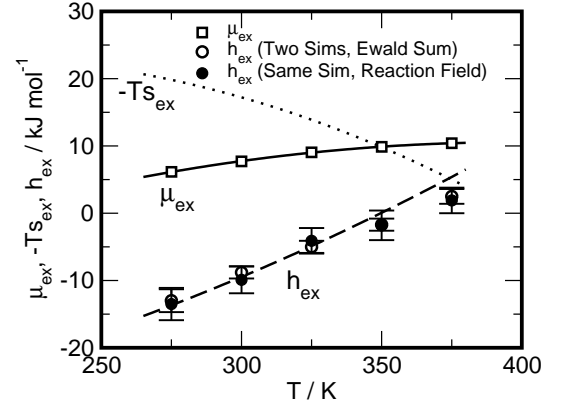


FIG. 1: Squares: Excess chemical potential of Xenon in SPCE water. Solid line: Cubic fit to the excess chemical potential of Xenon with respect to the temperature according to $\mu_{ex}(T) = \mu_0 + \mu_1 T + \mu_2 T^2$ with $\mu_0 = -35.90 \text{ kJ mol}^{-1}$, $\mu_1 = 2.33 \times 10^{-1} \text{ kJ mol}^{-1} \text{ K}^{-1}$ and $\mu_2 = -2.94 \times 10^{-4} \text{ kJ mol}^{-1} \text{ K}^{-2}$. Dotted line: Solvation entropy s_{ex} according to the fitted data. Dashed line: Solvation enthalpy h_{ex} according to the fitted data. Open circles: Solvation enthalpies obtained directly by subtracting the total configurational energies from simulations consisting of 500 SPCE + 1 Xenon molecules and simulations containing 500 SPCE molecules. The energy data are according to the particle mesh Ewald summation. Filled circles: Solvation enthalpies obtained from 500 SPCE + 1 Xenon simulations by using the individually calculated energies for the solute, shell water and bulk water. The energies are obtained by using the reaction field method discussed in the text.

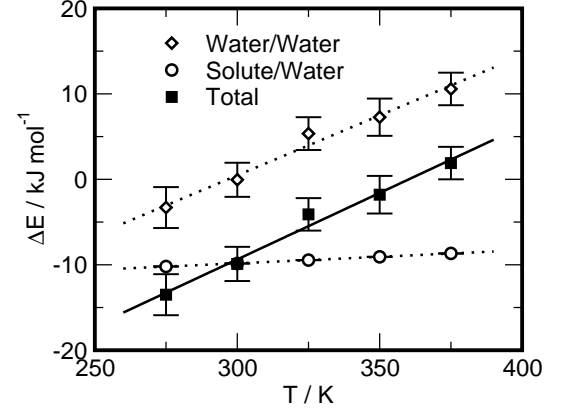


FIG. 2: Solvation enthalpies $\Delta E \equiv h_{ex}$ obtained from the 500 SPCE + 1 Xenon simulations by using the individually calculated energies for the solute, shell water and bulk water: $\Delta E_{\text{Solute/Water}} = E_{\text{solute}}$ and $\Delta E_{\text{Water/Water}} = n_{\text{shell}} \times (E_{\text{shell}} - E_{\text{bulk}})$. The open diamonds denote the Water/Water contribution, whereas the open circles indicate the Solute/Water contribution. The black squares indicate the sum of both contributions. The lines indicate the excess heat capacities: Solute/Water: $c_{P,ex} = 15.3 \text{ J K}^{-1} \text{ mol}^{-1}$; Water/Water: $c_{P,ex} = 140.3 \text{ J K}^{-1} \text{ mol}^{-1}$; Total $c_{P,ex} = 155.6 \text{ J K}^{-1} \text{ mol}^{-1}$.

SPCE water. The configurational energies shown in Table II were directly obtained from GROMACS during the simulation, employing the particle mesh Ewald summation technique (see section II A for details concerning the setup of the PME). The rather long simulation runs of 20 ns length provide us sufficiently accurate data to de-

| T/K | (500 SPCE) $\langle E_c \rangle / \text{kJ mol}^{-1}$ | (500 SPCE + 1 Xe) $\langle E_c \rangle / \text{kJ mol}^{-1}$ | $\langle \Delta E_c \rangle / \text{kJ mol}^{-1}$ |
|-------|--|---|---|
| 275 | -24073.6 ± 1.3 (-48.1472 ± 0.0026) | -24086.6 ± 1.0 | -13.0 ± 1.6 |
| 300 | -23288.1 ± 0.7 (-46.5762 ± 0.0014) | -23296.8 ± 0.7 | -8.8 ± 1.0 |
| 325 | -22531.2 ± 0.5 (-45.0624 ± 0.0010) | -22536.2 ± 0.8 | -5.0 ± 0.9 |
| 350 | -21794.3 ± 0.7 (-43.5886 ± 0.0014) | -21796.0 ± 0.6 | -1.7 ± 0.9 |
| 375 | -21071.2 ± 0.8 (-42.1424 ± 0.0016) | -21068.7 ± 0.8 | 2.5 ± 1.1 |

TABLE II: Left columns: Average configurational energies E_c as directly obtained from the simulations of 500 SPCE molecules with and without an additional Xenon particle. The values given in brackets denote the energy per molecule. The data corresponds to the Particle mesh Ewald summation, applying appropriate cutoff corrections for the Lennard-Jones contributions. Right column: The difference between the two energy contributions denotes the solvation enthalpy $h_{ex} \equiv \langle \Delta E_c \rangle$ for Xenon in SPCE water.

| T/K | $\langle E_{\text{solute}} \rangle / \text{kJ mol}^{-1}$ | $\langle E_{\text{shell}} \rangle / \text{kJ mol}^{-1}$ | $\langle n_{\text{shell}} \rangle$ | $\langle E_{\text{bulk}} \rangle / \text{kJ mol}^{-1}$ | $\langle \Delta E \rangle / \text{kJ mol}^{-1}$ |
|-------|--|---|------------------------------------|--|---|
| 275 | -10.196 ± 0.014 | -48.125 ± 0.016 | 137.50 ± 0.04 | -48.102 ± 0.007 | -13.5 ± 2.4 |
| 300 | -9.846 ± 0.014 | -46.527 ± 0.014 | 135.94 ± 0.03 | -46.527 ± 0.006 | -9.9 ± 2.0 |
| 325 | -9.453 ± 0.013 | -44.980 ± 0.013 | 133.97 ± 0.03 | -45.020 ± 0.005 | -4.1 ± 1.9 |
| 350 | -9.071 ± 0.012 | -43.489 ± 0.016 | 131.28 ± 0.04 | -43.545 ± 0.005 | -1.8 ± 2.2 |
| 375 | -8.672 ± 0.014 | -42.017 ± 0.014 | 128.18 ± 0.03 | -42.099 ± 0.005 | 1.9 ± 1.9 |

TABLE III: Potential energies of the solute particle and the water molecules obtained by using a cubic minimum image cutoff, a reaction field correction and a cubic Lennard-Jones cutoff correction, as outlined in the text. $\langle E_{\text{solute}} \rangle$ is the potential energy of the solute particle, $\langle E_{\text{shell}} \rangle$ is the average potential energy of the water molecules in the sphere of 1.0 nm radius around the solute particle. $\langle n_{\text{shell}} \rangle$ is the average number of water molecule in this sphere. $\langle E_{\text{bulk}} \rangle$ is the potential energy of the water molecules outside the solute sphere. The net solvation enthalpy is obtained as $h_{ex} \equiv \langle \Delta E \rangle = \langle E_{\text{solute}} \rangle + \langle n_{\text{shell}} \rangle \times (\langle E_{\text{shell}} \rangle - \langle E_{\text{bulk}} \rangle)$.

termine the hydration enthalpies with an errorbar of approximately $\pm 1 \text{ kJ mol}^{-1}$. A comparison of the directly obtained h_{ex} data with the hydration enthalpies determined from the solvation free-energies is given in Figure 1. The dashed curve, which is representing the hydration enthalpies according to the fitted $\mu_{ex}(T)$ data, is mostly lying within the errorbars of the directly obtained enthalpies (open symbols). However, the apparent deviation at 375 K might be attributed to the restriction of the fit of the μ_{ex} -data to the finite temperature interval between 275 K and 375 K.

As an alternative to the *two simulations* approach, we calculate the solvation enthalpy based on the “individual” potential energies of solute and solvent molecules using the reaction field method discussed in section II C. Table III contains the energies of the solute molecule E_{solute} and the water molecules in the bulk and in the hydration sphere of radius 1.0 nm, as well as the number of the water molecules in the hydration sphere. A comparison of the energy values for the water bulk using the reaction field with the data for the pure water system according to the Ewald summation (given in Table II) reveals that the reaction field data are lying systematically about

$0.042 \text{ kJ mol}^{-1}$ higher than the Ewald data. Although being rather small, this noticeable difference is of systematic nature and is presumably due to the lack of higher order multipole contributions to the reaction field term, which are, of course, present in the Ewald calculation [58]. However, the differences apparently cancel out when considering energy differences between shell and bulk, when determining the solvation enthalpies. As shown in Figure 1 and Tables II and III, the obtained data for h_{ex} is, both, consistent with the *two simulations* solvation enthalpies, as well as the solvation enthalpies obtained from the temperature dependence of the solvation free energies. Figure 2 reports a division of the solvation enthalpy h_{ex} (total) into contributions according to the solute $\langle E_{\text{solute}} \rangle$ (Solute/Water) and the solvent $h_{ex} - \langle E_{\text{solute}} \rangle$ (Water/Water). The calculated total excess heat capacity $c_{P,ex}$ of $155.6 \text{ J K}^{-1} \text{ mol}^{-1}$ is dominated by the Water/Water contribution of $140.3 \text{ J K}^{-1} \text{ mol}^{-1}$, whereas the Solute/Water part with $15.3 \text{ J K}^{-1} \text{ mol}^{-1}$ contributes only to about 10%. The observed value for $c_{P,ex}$ of $155.6 \text{ J K}^{-1} \text{ mol}^{-1}$, however, does only qualitatively agree with the value of about $280 \text{ J K}^{-1} \text{ mol}^{-1}$, observed experimentally for $T = 300 \text{ K}$ [36, 59]. We would also like

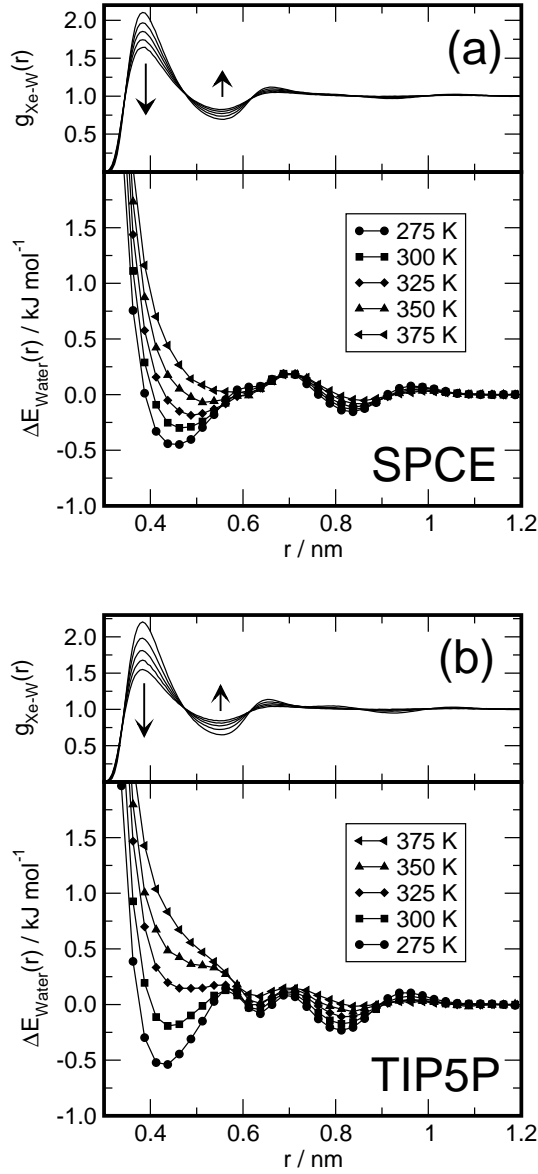


FIG. 3: Xenon-Water center of mass pair distribution function $g_{\text{Xe-W}}(r)$ and relative change of the water potential energy $\Delta E_{\text{Water}}(r) = E_{\text{Water}}(r) - E_{\text{Water}}^{\text{bulk}}$ for all investigated temperatures. The arrows indicate the sequence of the $g(r)$ -curves pointing from low to high temperatures. a. SPCE model b. TIP5P model.

to point out that the experimentally observed increase of the excess heat capacity with decreasing temperature (as discussed in Ref. [3]) seems not to be present in the SPCE simulation data. However, the change of the Xenon solvation enthalpy from negative to positive at about 363 K has to be attributed mainly to the potential energy change of the of water molecules in the hydrophobic hydration shell. In order to elucidate the spacial (radial) extension of the solvent contribution to the excess heat capacity, we calculate the potential energy of the water molecules as a function of distance to the Xenon atom. Figure 3 shows the change of the potential energy of the water molecules around a Xenon particle with re-

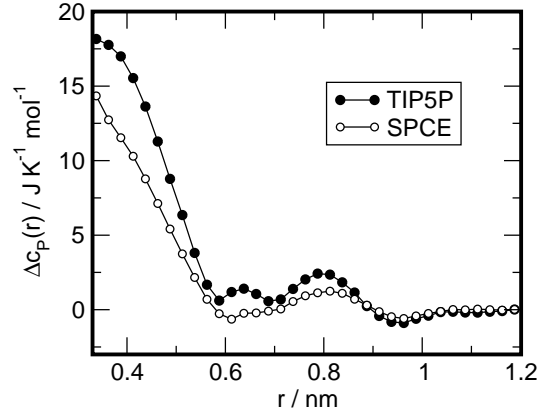


FIG. 4: Change of the heat capacity of the water molecules around a Xenon particle $\Delta c_P(r) = c_P(r) - c_P^{\text{bulk}}$ as a function of distance to the Xenon particle. The $\Delta c_P(r)$ is obtained as a linear regression of the datasets shown in Figure 3.

spect to the bulk value for the SPCE and TIP5P models as a function of temperature. Due to the better statistics, the data in Figure 3 were obtained from the simulations containing 8 Xenon particles. For completeness, also the Xenon-Water center of mass pair distribution functions are indicated. A rather strong temperature dependence of the potential energy of the water molecules in the first hydration shell is clearly evident for both models. A rather remarkable observation is, that for the lower temperatures the water molecules in the distance interval between 0.4 nm and 0.5 nm, which are corresponding to the first hydration shell, exhibit a potential energy even lower than the bulk value. With increasing temperature this behavior is reversed and the location of the molecules in the hydration shell becomes more and more energetically unfavorable. On a qualitative level, both the SPCE and TIP5P model, exhibit a similar behavior. The TIP5P model, however, shows a more strongly pronounced temperature dependence, and a more richly structured potential energy profile. We would like to emphasize that for the SPCE model at the lowest temperature we find an average potential energy for the water molecules in the hydration sphere, which lies *below* the average bulk value (see Table III). The fact that Durell and Wallqvist did not observe this in their simulations [57] is perhaps due to their restricted temperature interval (300 K to 350 K).

The temperature dependence of the distance dependent water potential energies are quantified in terms of the configurational heat capacity. Figure 4 shows the water heat capacities as a function of the distance to the Xenon particle. The data are given relative to the value for the water bulk of $60.0 \text{ J K}^{-1} \text{mol}^{-1}$, obtained for the SPCE model, and $90.8 \text{ J K}^{-1} \text{mol}^{-1}$, obtained for the TIP5P model. As already evident from Figure 3, the strongest heat capacity effect is observed for the first hydration shell. For the TIP5P model a noticeably enhanced heat capacity is also observed for the distance range between 0.6 nm and 1.0 nm. Beyond a separation

distance of 1.0 nm, however, no significant energy difference compared to the bulk can be denoted, indicating a properly chosen size of the solvation sphere used for the calculation of the hydration enthalpies h_{ex} .

B. Hydrophobic Interaction

The hydrophobic interaction between two Xenon particles is obtained as a profile of free energy $w(r)$ for the association of Xenon particles from the simulations containing 8 Xenon particles. The $w(r)$, as well as the corresponding enthalpic and entropic contributions $h(r)$ and $-Ts(r)$ are shown in Figure 5. For both water models the “contact state” is defined by the minimum of the $w(r)$ function at a distance of about 0.42 nm. With increasing temperature the well depth of the minimum of the profile of free energy at the contact state drops from about $-2.21 \text{ kJ mol}^{-1}$ (275 K) to $-4.25 \text{ kJ mol}^{-1}$ (375 K) for the SPCE model and $-1.36 \text{ kJ mol}^{-1}$ (275 K) to $-4.02 \text{ kJ mol}^{-1}$ (375 K) for the TIP5P model. The accuracy for each of the $w(r)$ profiles has been determined to be about $\pm 0.15 \text{ kJ mol}^{-1}$. The contact state minimum and the minimum characterizing the solvent separated

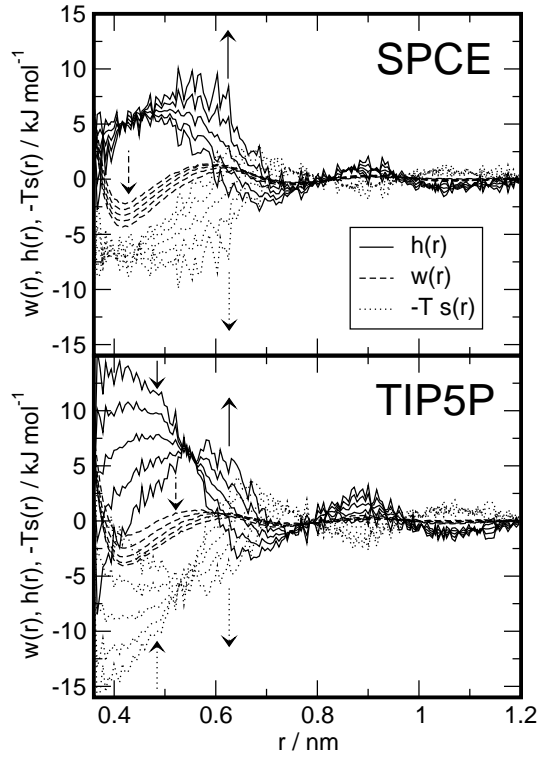


FIG. 5: Profiles of free energy $w(r)$ obtained for the association of two Xenon particles (dashed lines) as well as their enthalpic and entropic contributions $w(r) = h(r) - Ts(r)$ for all five temperatures (275 K, 300 K, 325 K, 350 K, 375 K). Solid lines: $h(r)$. Dotted lines: $-Ts(r)$ Top: SPCE model; Bottom: TIP5P model. The arrows indicate the sequence of the data curves pointing from low to high temperatures. The data shown here is identical to the data presented in Ref. [36].

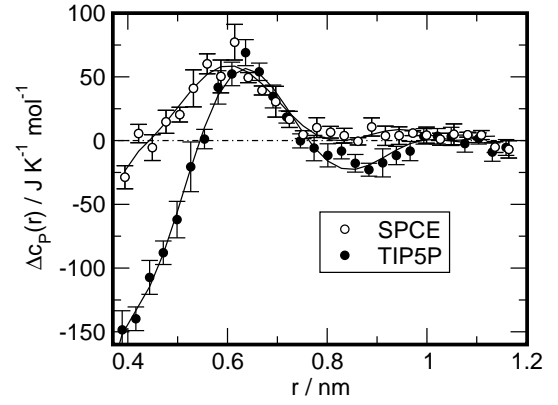


FIG. 6: Relative change in heat capacity $\Delta c_P(r) = c_P(r) - c_P^{bulk}$ for the hydrophobic interaction between two dissolved Xenon particles using the SPCE and TIP5P models. The data correspond to the temperature derivative of quadratic fits of $w(r, T)$ obtained for 300 K. The solid lines are just to guide the eye. The data shown here is identical to the data reported in Ref. [36].

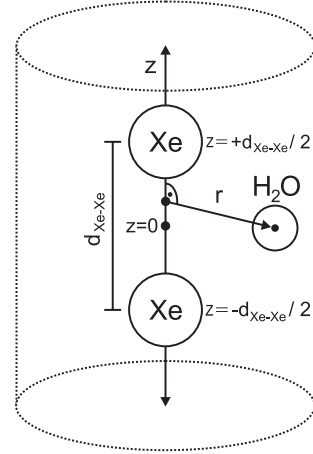


FIG. 7: Schematic illustration of the employed definition for the cylindrical distribution of the water density and heat capacity around a pair of Xenon particles obtained for different Xenon-Xenon separation distances d_{Xe-Xe} .

state, which is located at a distance of about 0.72 nm to 0.78 nm, are separated by the so called *desolvation barrier*, which is found approximately at a distance of 0.6 nm. Figure 5 indicates that for lower temperatures the contact state is entropically stabilized and enthalpically destabilized, in accordance with the observation of Smith and Haymet [8, 9] and others [16, 21, 23, 24, 28]. For the TIP5P model, we observe a strong temperature dependence of the curves, showing a decrease of the absolute values for the enthalpy and entropy contributions. In contrast to the TIP5P model, the SPCE model does exhibit only a weak temperature dependence of $h(r)$ and $-Ts(r)$ at the contact state. At the desolvation barrier, however, the inverse behavior is observed for both models: with increasing temperature the entropy/enthalpy compensation effect is found to be enlarged.

The observed temperature dependence of the enthalpy

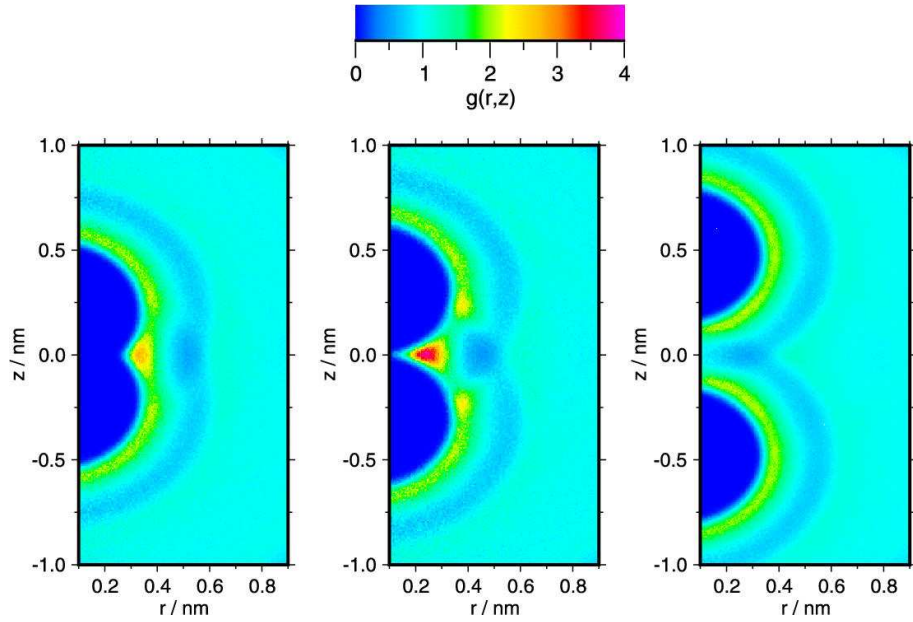


FIG. 8: Cylindrical distribution function of the SPCE water molecules center of mass around a pair of Xenon particles $g_{\text{Xe-Xe-w}}(r, z)$ obtained for a certain Xe-Xe distance interval at $T=300$ K. Left: “contact” ($d_{\text{Xe-Xe}} \leq 0.45$ nm). Middle: “desolvation barrier” ($0.55 \text{ nm} \leq d_{\text{Xe-Xe}} \leq 0.65$ nm). Right: “separated” ($0.9 \text{ nm} \leq d_{\text{Xe-Xe}} \leq 1.0$ nm).

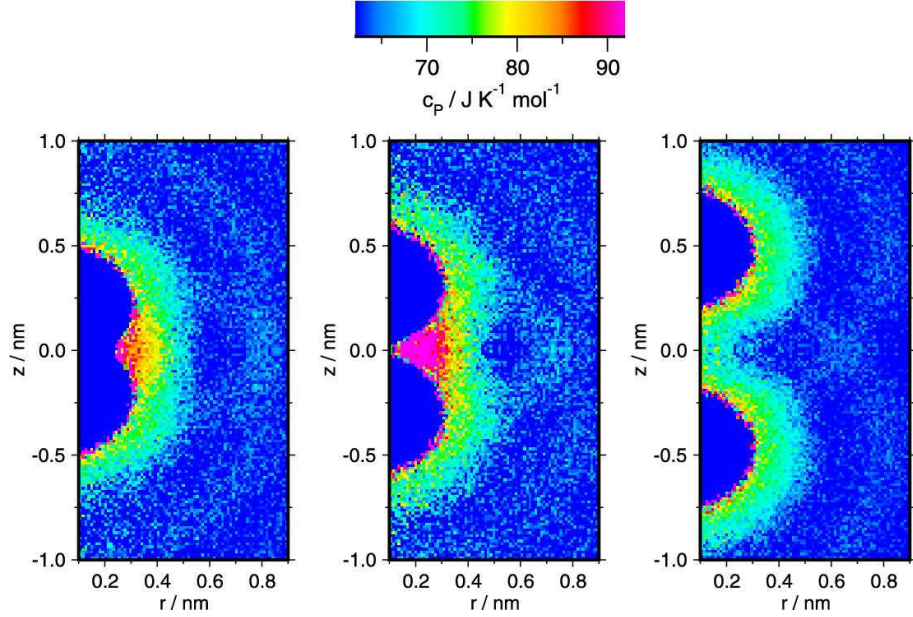


FIG. 9: Cylindrical distribution function of the configurational contribution to the heat capacity of the SPCE water molecules around a pair of Xenon particles $c_P(r, z)$ obtained for a certain Xe-Xe distance interval. The $c_P(r, z)$ data have been obtained as linear fits to the corresponding water potential energies $E_{\text{Water}}(r, z)$ for all five temperatures. The average bulk value is $62.1 \text{ J K}^{-1} \text{ mol}^{-1}$. Left: “contact” ($d_{\text{Xe-Xe}} \leq 0.45$ nm). Middle: “desolvation barrier” ($0.55 \text{ nm} \leq d_{\text{Xe-Xe}} \leq 0.65$ nm). Right: “separated” ($0.9 \text{ nm} \leq d_{\text{Xe-Xe}} \leq 1.0$ nm).

profiles is quantified in terms of a heat capacity profile for the association of two Xenon particles, shown in Figure 6. In accordance with the observations of Shimizu and Chan [23, 25, 26], and Rick [30], we observe a maximum of the heat capacity located at the desolvation barrier. For the contact state, however, the two water models employed in our study show a quite different behavior.

For the SPCE model we find almost no difference in the heat capacity between the contact state and the completely separated state, corresponding to the observation of Shimizu and Chan [25, 26] for Methane in TIP4P water. For the TIP5P model, however, we observe a considerable negative heat capacity contribution at the contact state.

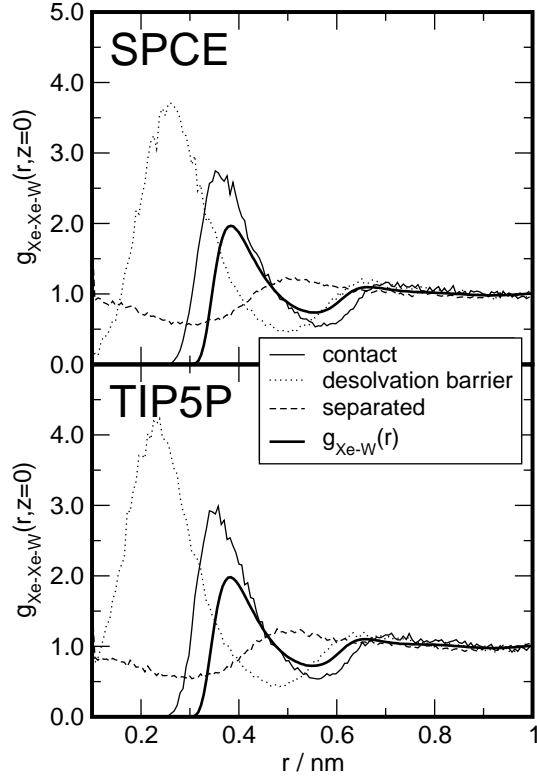


FIG. 10: Distribution function of the SPCE water molecules center of mass around a pair of Xenon particles in the Xe-Xe bisector plane $g_{\text{Xe-Xe-W}}(r, z=0)$ obtained for a certain Xe-Xe distance interval at $T=300$ K. “contact”: $d_{\text{Xe-Xe}} \leq 0.45$ nm. “desolvation barrier”: $0.55 \text{ nm} \leq d_{\text{Xe-Xe}} \leq 0.65$ nm. “separated”: $0.9 \text{ nm} \leq d_{\text{Xe-Xe}} \leq 1.0$ nm. For comparison, also the Xe-W pair distribution functions are given. Top: SPCE model. Bottom: TIP5P model.

At a first glance this behavior can be rationalized as a simple consequence of the overlapping of the hydration shells in case two hydrophobic particles approach each other. The positive association enthalpy and entropy corresponds to a picture of the release of shell water molecules with a lower potential energy and higher ordering into the bulk phase. However, when taking the temperature dependence of the $h(r)$ and $s(r)$ profiles into account, two observations are *not* consistent with this simple model considerations: First, since the hydration shell water molecules have been shown to exhibit an enhanced heat capacity, a reduced number of water molecules in the joint hydration shell of a pair of Xenon atoms in the contact state should also lead to a net negative heat capacity. This, however, is apparently not the case for the SPCE model. The second obvious inconsistency is, of course, the enlarged positive heat capacity observed at desolvation barrier, found for both water models here, and even more water models, as discussed in Ref. [36].

In order to elucidate the observed heat capacity profile for the Xenon-Xenon association, we calculate two-dimensional distribution functions describing the water density as well as the water heat capacity around a pair of Xenon particles, found at a certain distance $d_{\text{Xe-Xe}}$.

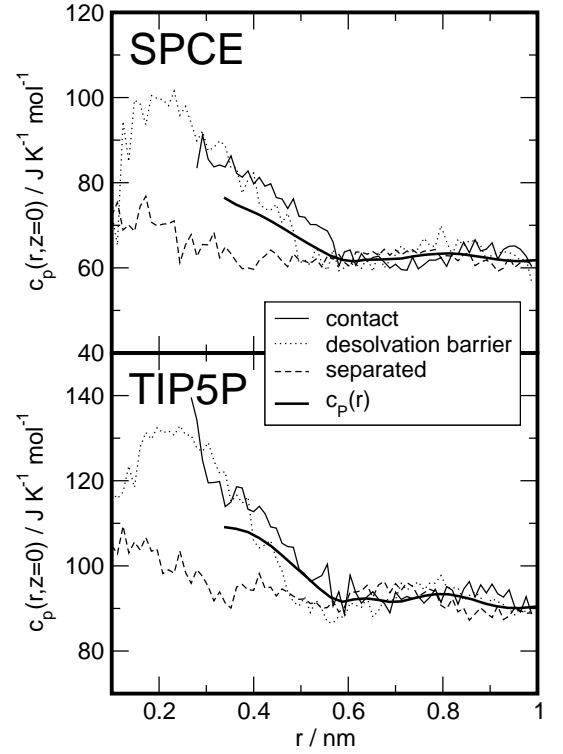


FIG. 11: Heat capacity of the SPCE water molecules around a pair of Xenon particles in the Xe-Xe bisector plane $c_p(r, z=0)$ obtained for a certain Xe-Xe distance interval. The $c_p(r, z=0)$ data have been obtained as linear fits to the corresponding water potential energies $E_{\text{Water}}(r, z=0)$ using all five temperatures. “contact”: $d_{\text{Xe-Xe}} \leq 0.45$ nm. “desolvation barrier”: $0.55 \text{ nm} \leq d_{\text{Xe-Xe}} \leq 0.65$ nm. “separated”: $0.9 \text{ nm} \leq d_{\text{Xe-Xe}} \leq 1.0$ nm. For comparison, also the $\Delta c_p(r) + c_{p,\text{bulk}}$ data of Figure 4 are given. Top: SPCE model. Bottom: TIP5P model.

These distributions are shown in Figures 8 and 9. Figure 7 illustrates the definition of distribution functions. We would like to point out that a conceptually similar plot of the molecule densities around a pair of hydrophobic Methane particles has been recently reported by Gosh et al. [28, 29]. If a pair of Xenon atoms is found to belong to a certain distance $d_{\text{Xe-Xe}}$ interval corresponding to one of the states “contact”, “desolvation barrier”, or “separated” (see the figure captions of Figures 8 and 9 for the corresponding definition intervals), the properties of the surrounding water molecules (normalized density, potential energy) are mapped with respect to their cylindrical coordinates r and z . $z=0$ is chosen in such a way that it indicates the bisector plane between the two adjacent Xenon particles.

Figure 8 shows the normalized cylindrical distribution functions of the water molecule density around a pair of Xenon atoms $g_{\text{Xe-Xe-W}}(r, z)$, obtained from the SPCE-Xenon simulations at 300 K. In order to provide a more quantitative comparison of the TIP5P and the SPCE models, we show in Figure 10 the distribution functions obtained for the bisector plane $g_{\text{Xe-Xe-W}}(r, z=0)$. Figure 8 reveals an enhanced water molecule density in the

range where the hydration shells of the two Xenon particles overlap. With $d_{\text{Xe-Xe}} \rightarrow 0$ the $g_{\text{Xe-Xe-W}}(r, z=0)$ function approaches the $g_{\text{Xe-W}}(r)$ pair correlation function. With increasing $d_{\text{Xe-Xe}}$ the first peak starts to increase showing roughly a doubled height (with respect to the first peak of $g_{\text{Xe-W}}(r)$) of the first maximum at the desolvation barrier. A further increase of $d_{\text{Xe-Xe}}$ leads again to a decrease in height of the first peak. This is qualitatively in accord with the observations of Ghosh et al. [29] obtained for Methane in TIP3P water. We find that both water model models show qualitatively the same behavior. The TIP5P model, however, exhibits a slightly stronger increase of the first peak at the desolvation barrier.

The heat capacity of the SPCE water around a pair of Xenon particles $c_P(r, z)$ is shown in Figure 9. The data were obtained by sampling the water potential energies as a function of r and z for all temperatures and subsequent linear fitting of the average values with respect to the temperature. The potential energies of the water molecules were obtained the same way as discussed in the previous sections. The color coding in Figure 9 is chosen in such a way that the lower limit coincides with the average bulk value for water's configurational heat capacity of $62.1 \text{ J K}^{-1} \text{ mol}^{-1}$. Since we consider here a system consisting of 8 Xenon particles and 500 water molecules, the bulk value for c_P of water is slightly larger than the value obtained for pure water discussed in section III A. The color spectrum represents a total range of $30 \text{ J K}^{-1} \text{ mol}^{-1}$. Figure 3 indicates that virtually no water molecules are found at distances smaller than about 0.3 nm to any Xenon site, hence no water c_P data is available. Therefore this region is represented in Figure 9 by the color indicating the lower limit for c_P . In order to provide a more quantitative representation, Figure 11 shows the heat capacity of the SPCE and TIP5P water molecules in the bisector plane.

Figure 9 reveals the origin the heat capacity maximum at the desolvation barrier, shown in Figure 6. The water molecules adsorbed close to the bisector plane between the two hydrophobic particles exhibit an about 60 % increased heat capacity (in the “desolvation barrier” state), which apparently overcompensates the effect of the shrinking of the total hydration shell. In addition, Figure 9 shows that the increased heat capacity of the hydration shell water molecules located in the bisector plane persists in the contact state, still partially compensating the reduced solvent accessible surface. The differences observed for the contact state of the TIP5P and SPCE models seem to be related to the individual strengths of these compensating effects. Figure 11 indicates that the SPCE and TIP5P models behave qualitatively similar. Even the relative changes are of the same size: The maximum at the desolvation barrier shows an increase of the heat capacity of about $40 \text{ J K}^{-1} \text{ mol}^{-1}$ for both water models. However, the TIP5P water exhibits an about $30 \text{ J K}^{-1} \text{ mol}^{-1}$ larger bulk heat capacity. As a consequence, the effect due to the decrease of the solvent

accessible surface has to be stronger in case of TIP5P, which might explain the negative heat capacity at the contact state. In addition, the heat capacity effect might as well be influenced by the second hydration shell of Xenon (see Figure 4). The heat capacity of the water in the second hydration shell is clearly more strongly affected in case of the TIP5P model. The contribution of this extended hydration shell should also lead to a more negative net excess heat capacity. The observed water heat capacities provide an explanation for the maximum of the heat capacity profile of two associating hydrophobic particles. Hence the differences between the SPCE and TIP5P models seem to be related to the delicate balance of two compensating effects: the reduction of the solvent accessible surface and the increased heat capacity of the water molecules in the concave part of the joint Xenon-Xenon hydration shell.

C. Hydrogen Bonding

Finally we would like to discuss the origin of the observed heat capacity effects. Therefore we calculate the (binding) molecule pair energies E_{pair} between water molecules which are potentially hydrogen bonded in the sense that their O-O distance is smaller than 0.35 nm

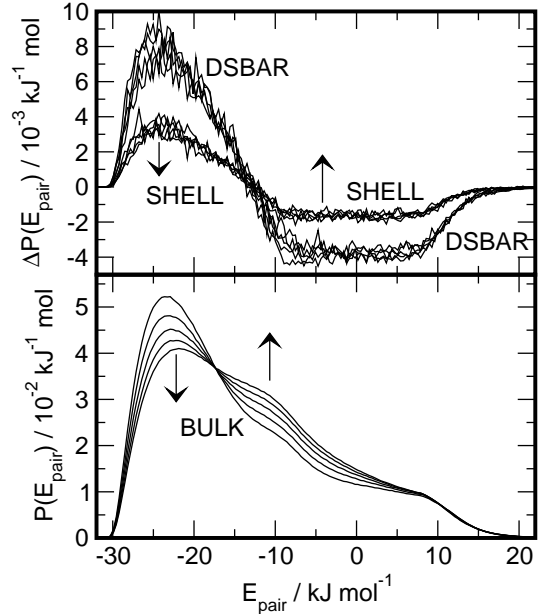


FIG. 12: Bottom: Probability density of observing a water-water pair energy of water molecules which are separated less than 0.35 nm , and which are located in the “BULK” phase. Top: Difference between the corresponding probability densities of water molecules belonging to the Xenon hydration shell (“SHELL”), as well as close to the bisector plane between two Xenon particles located at the desolvation barrier (“DSBAR”), and the probability density obtained for the bulk (exact definitions are given in the text). The arrows indicate the sequence of curves pointing from low to high temperatures.

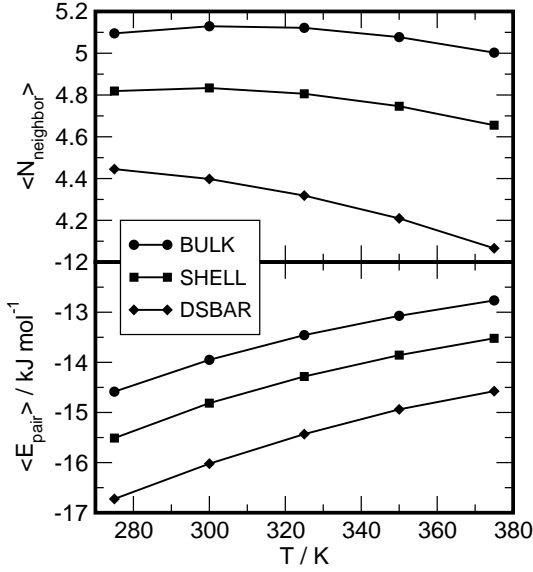


FIG. 13: Top: Average number of nearest (water) neighbors of a SPCE molecule. Bottom: Average nearest neighbor pair interaction energies of a SPCE water molecule belonging to the states “BULK”, “SHELL”, and “DSBAR” (Definitions are given in the text).

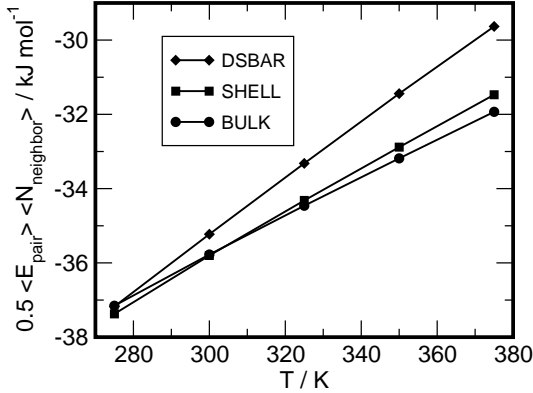


FIG. 14: Potential energy of a water molecule according to nearest neighbor interactions (applying an oxygen-oxygen cutoff of $r_c = 0.35$ nm) belonging to the states “BULK”, “SHELL”, and “DSBAR”.

[10, 61]. For this purpose we distinguish between three distinct states: “BULK”: The separation from the hydrophobic particle is larger than 1.0 nm. “SHELL”: The water molecules are found to lie within a sphere with radius 0.55 nm around the hydrophobic particle. “DSBAR”: The water molecules are found in the region close to the bisector plane between two adjacent Xenon particles found within the distance interval between $0.55 \text{ nm} \leq d_{\text{Xe-Xe}} \leq 0.65 \text{ nm}$, in the region defined by $r \leq 0.4 \text{ nm}$ and $-0.15 \text{ nm} \leq z \leq 0.15 \text{ nm}$ (see Figures 7 and 8 for further explanations). For the first two categories we employ simulations containing a single Xenon atom, whereas for the “DSBAR” category we use the simulations with 8 Xenon particles. We would like to point out that the

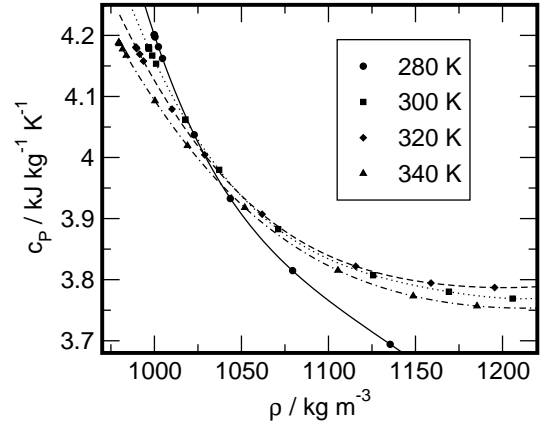


FIG. 15: Symbols: Heat capacity c_p data of pure water as a function of density according to the IAPWS-95 formulation [60] (Data are taken from Ref. [60]). Lines: 5th order polynomial fits of the $c_p(\rho)$ data.

simulations containing 8 Xenon atoms provide qualitatively similar results for the first two categories. All data reported in this section were obtained using the SPCE model, but the TIP5P model is found to furnish a qualitatively similar picture.

In Figure 12 the probability densities for obtaining a certain water-water pair energy $P(E_{\text{pair}})$ are given. Comparing the “SHELL” state with the “BULK” state we find an increased population of states with binding energies less than approximately -12 kJ mol^{-1} . Interestingly, the water molecules in the “DSBAR” state show an *even more* enhanced population of strongly bound water molecules. A noteworthy observation is that the temperature variation of the probability density distributions of the “SHELL” and “DSBAR” states with respect to the bulk is found to be only small. At least, significantly smaller than bringing a water molecule in either the “SHELL” or “DSBAR” state. Figure 13 contains the obtained average pair energies, indicating that the binding energies according to the “SHELL” and “DSBAR” states are shifted to lower values. A consequence of the small temperature variation of the water-water probability density is that the energy averages $\langle E_{\text{pair}} \rangle$ for the three different states are running mostly parallel to the bulk data. A second parameter controlling the potential energy of the water molecules is, of course, the number of possible binding partners, or number of nearest neighbors $\langle N_{\text{neighbor}} \rangle$. Figure 13 therefore shows the number of nearest neighbors as a function of temperature. To obtain a first order approximation to the water potential energy we may just consider the first solvation shell of each water molecule, according to $E \approx 1/2 \langle E_{\text{pair}} \rangle \times \langle N_{\text{neighbor}} \rangle$. The corresponding energy data are shown in Figure 14. The temperature dependence reveals that the water heat capacity effects discussed in sections III A and III B have to be largely attributed to the waters nearest environment. The heat capacities according to the data shown

in Figure 14 are $52.1 \text{ J K}^{-1} \text{ mol}^{-1}$, $58.9 \text{ J K}^{-1} \text{ mol}^{-1}$, and $75.5 \text{ J K}^{-1} \text{ mol}^{-1}$ for “BULK”, “SHELL”, and “DSBAR”, respectively, hence accounting for about 85 % of the heat capacity considering the full environment. We would like to stress two observations: The reduction of the number of water neighbors, i.e. reduction of the local water density, leads apparently to a strengthening of the water/water pair interactions. We would like to emphasize that this behavior is analogous to the behavior observed for stretched water [62, 63, 64, 65, 66], as well as to the behavior found in low density patches due to density fluctuations of water at ambient conditions [63, 64]. In Ref. [63] and [64] Sciortino et al. showed that a decrease in density is accompanied by a strengthened water-water binding energy. As mechanism they identify a decreasing amount of “fifth neighbor” configurations, contributing energetically unfavorable “bifurcated” hydrogen bonds. The same behavior is observed in the hydrophobic hydration shell. Hence the water in the “SHELL” and “DSBAR” states might be considered as *locally stretched* water, while representing different degrees of stretching. The increased heat capacity with stretching is also consistent with the experimentally obtained heat capacity of pure water based on the IAPWS-95 formulation according to Wagner and Pr   [60]. The density dependence of the heat capacities are shown in Figure 15 for several temperatures. As a rough estimate we obtain $(\partial c_P(\rho)/\partial \rho)_T = -5.5 \times 10^3 \text{ kJ m}^3 \text{ kg}^{-2} \text{ K}^{-1}$ for $T = 300 \text{ K}$ around $\rho = 1000 \text{ kg m}^{-3}$. The configurational contribution to the heat capacity might be approximated as $c_P(\text{liq.}) - c_P(\text{gas}) \approx 2.27 \text{ kJ kg}^{-1} \text{ K}^{-1}$. Hence a density decrease of about 14%, as found for the “DSBAR” state, should lead to an increase of the configurational heat capacity of about 34%. A density decrease of about 7%, as observed for the “SHELL” region, should result in a heat capacity increase of about 17%. Both are quite close to the observed simulation data. In accordance with recent ideas of Ashbaugh et al. [67], the effects of the hydrophobic hydration and interaction discussed here might therefore simply reflect features of water’s unique equation of state.

Our simulations indicate that the water-water binding energy-decrease counterbalances (and at lower temperature even overcompensates) the effect of the dilution of water molecules in the vicinity of hydrophobic particles. With increasing temperature the apparent enhanced disintegration of the water network (number of nearest neighbors in Figure 14) close to hydrophobic particles is therefore responsible for the observed heat capacity effects. To illustrate this, we finally discuss hydrogen bonding based on a topological criterion. A pair of water molecules is considered to be “hydrogen bonded” when the O-O distance is smaller than 0.35 nm and the $\text{H}-\text{O}\cdots\text{O}$ angle is smaller than 30° [61, 68]. Each water hydrogen is considered to be a hydrogen bond donor and f_{HB} denotes the fraction of hydrogen bond donors which are *not* involved in a hydrogen bond, or the fraction of broken hydrogen bonds. f_{HB} as a function of

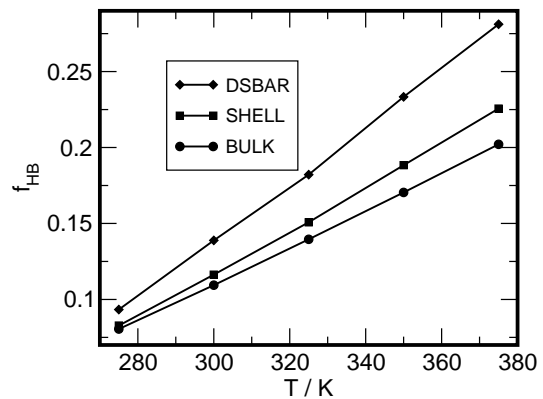


FIG. 16: Fraction of broken hydrogen bonds f_{HB} for water molecules belonging to the states “BULK”, “SHELL”, and “DSBAR”.

temperature is shown in Figure 16 for water molecules belonging to different states. In parallel with observed increasing potential energies, the increasing temperature leads to an enhanced breaking of hydrogen bonds. This effect is found to be enhanced in the hydration shell of the hydrophobic particles and particularly strong for water molecules in the “DSBAR” state.

IV. CONCLUSIONS

We have shown that for simple hydrophobic solutes the observed positive excess heat capacity of solvation is largely (about 90%) determined by an increase of the heat capacity of the water in the first hydration shell. The effect is mainly attributed to the altered potential energy of the water molecules in the first hydration shell, changing their energy state from “attractive” at lower temperatures to “repulsive” at higher temperatures. The two model systems studied, SPCE and TIP5P water, show a qualitatively similar behavior, although the effect is found to be quantitatively stronger in case of the TIP5P model.

Our model calculations, in accordance with the calculations of Shimizu and Chan [23, 25, 26], as well as Rick [30] and Paschek [36], indicate that the heat capacity for the association of two hydrophobic particles exhibits a maximum located at the desolvation barrier. Our simulations indicate that this seems to be a characteristic feature of the hydrophobic interaction of small apolar particles. The observed behavior is found to be a counterplay of two effects: The reduced solvent accessible surface, and the increased heat capacity of water molecules located in the gap between the two hydrophobic particles. In case of the SPCE model, the water molecules located in this bridging situation show a heat capacity increase of about 60 % compared to the bulk, apparently overcompensating the effect of a reduced solvent accessible surface. The differences found for the SPCE and TIP5P models in the contact state are accordingly re-

lated to quantitative differences in strength of this two compensating effects.

A detailed analysis of the water-water pair interactions in the different states (bulk, hydration shell, joint hydration shell of two Xenon atoms) reveals that the observed heat capacity effects can be rationalized as a counterbalance of strengthened hydrogen bonds and an enhanced disintegration of the hydrogen bond network with increasing temperature. The reduced number of water neighbors in the different parts of the joint hydrophobic hydration shell might be interpreted as a *locally stretched* water/hydrogen bond network. A comparison with experimental data indicates that the observed heat capacity effects have the same order of magnitude as it would be

expected for pure water with an approximately equally reduced density.

ACKNOWLEDGEMENT

I would like to thank Alfons Geiger and Ivan Brovchenko for insightful discussions. The analogy between hydration shell water and stretched water has been originally suggested by Alfons Geiger. Financing by the Deutsche Forschungsgemeinschaft (DFG Forschergruppe 436) is gratefully acknowledged.

-
- [1] C. Tanford, *The Hydrophobic Effect: Formation of Micelles and Biological Membranes* (John Wiley & Sons, New York, 1980), 2nd ed.
 - [2] A. Ben-Naim, *Hydrophobic Interactions* (Plenum Press, New York, 1980).
 - [3] N. T. Southall, K. A. Dill, and A. D. J. Haymet, *J. Phys. Chem. B* **106**, 521 (2002).
 - [4] N. Muller, *Acc. Chem. Res.* **23**, 23 (1990).
 - [5] B. Lee and G. Graziano, *J. Am. Chem. Soc.* **118**, 5165 (1995).
 - [6] S. Moelbert and P. De Los Rios, *J. Chem. Phys.* **119**, 7988 (2003).
 - [7] S. Moelbert and P. De Los Rios, *Macromolecules* **36**, 5845 (2003).
 - [8] D. E. Smith, L. Zhang, and A. D. J. Haymet, *J. Am. Chem. Soc.* **114**, 5875 (1992).
 - [9] D. E. Smith and A. D. J. Haymet, *J. Chem. Phys.* **98**, 6445 (1993).
 - [10] A. Geiger, A. Rahman, and F. H. Stillinger, *J. Chem. Phys.* **70**, 263 (1979).
 - [11] D. A. Zichi and P. J. Rossky, *J. Chem. Phys.* **83**, 797 (1985).
 - [12] D. A. Pearlman, *J. Chem. Phys.* **98**, 8946 (1993).
 - [13] D. van Belle and S. J. Wodak, *J. Am. Chem. Soc.* **115**, 647 (1993).
 - [14] L. X. Dang, *J. Chem. Phys.* **100**, 9032 (1994).
 - [15] J. Forsman and B. Jönsson, *J. Chem. Phys.* **101**, 5116 (1994).
 - [16] S. Lüdemann, H. Schreiber, R. Abseher, and O. Steinhauser, *J. Chem. Phys.* **104**, 286 (1996).
 - [17] N. T. Skipper, C. H. Bridgeman, A. D. Buckingham, and R. L. Mancera, *Faraday Discuss.* **103**, 141 (1996).
 - [18] W. S. Young and C. L. Brooks III., *J. Chem. Phys.* **106**, 9265 (1997).
 - [19] G. Hummer, S. Garde, A. E. Garcia, A. Pohorille, and L. R. Pratt, *Proc. Natl. Acad. Sci. USA* **93**, 8951 (1996).
 - [20] S. Lüdemann, R. Abseher, H. Schreiber, and O. Steinhauser, *J. Am. Chem. Soc.* **119**, 4206 (1997).
 - [21] S. W. Rick and B. J. Berne, *J. Phys. Chem. B* **101**, 10488 (1997).
 - [22] G. Hummer, *J. Chem. Phys.* **114**, 7330 (2001).
 - [23] S. Shimizu and H. S. Chan, *J. Chem. Phys.* **113**, 4683 (2000).
 - [24] S. W. Rick, *J. Phys. Chem. B* **104**, 6884 (2000).
 - [25] S. Shimizu and H. S. Chan, *J. Am. Chem. Soc.* **123**, 2083 (2001).
 - [26] S. Shimizu and H. Chan, *Proteins: Struct., Funct., Genet.* pp. 560–566 (2002).
 - [27] T. Ghosh, A. E. Garcia, and S. Garde, *J. Am. Chem. Soc.* **123**, 10997 (2001).
 - [28] T. Ghosh, A. E. Garcia, and S. Garde, *J. Chem. Phys.* **116**, 2480 (2002).
 - [29] T. Ghosh, A. E. Garcia, and S. Garde, *J. Phys. Chem. B* **107**, 612 (2003).
 - [30] S. W. Rick, *J. Chem. Phys. B* **107**, 9853 (2003).
 - [31] B. Lee and F. M. Richards, *J. Mol. Biol.* **55**, 379 (1971).
 - [32] G. I. Makhatadze and P. L. Privalov, *Adv. Protein Chem.* **47**, 307 (1995).
 - [33] L. R. Pratt, *Annu. Rev. Phys. Chem.* **53**, 409 (2003).
 - [34] B. Widom, P. Bhimalapuram, and K. Koga, *Phys. Chem. Chem. Phys.* **5**, 3085 (2003).
 - [35] D. E. Smith and A. D. J. Haymet, in *Reviews in Computational Chemistry*, edited by K. B. Lipkowitz, R. Larter, and T. R. Cundari (Wiley-VCH, New York, 2003), vol. 19, chap. 2, pp. 44–77.
 - [36] D. Paschek, *J. Chem. Phys.* (2004), accepted for publication (Preprint: cond-mat/0312252).
 - [37] S. Nosé, *Mol. Phys.* **52**, 255 (1984).
 - [38] W. G. Hoover, *Phys. Rev. A* **31** (1985).
 - [39] A. R. M. Parrinello, *J. Appl. Phys.* **52**, 7182 (1981).
 - [40] S. Nosé and M. L. Klein, *Mol. Phys.* **50**, 1055 (1983).
 - [41] U. Essmann, L. Perera, M. L. Berkowitz, T. A. Darden, H. Lee, and L. G. Pedersen, *J. Chem. Phys.* **103**, 8577 (1995).
 - [42] S. Miyamoto and P. A. Kollman, *J. Comp. Chem.* **13**, 952 (1992).
 - [43] E. Lindahl, B. Hess, and D. van der Spoel, *J. Mol. Mod.* **7**, 306 (2001).
 - [44] D. van der Spoel, A. R. van Buuren, E. Apol, P. J. Meulenhoff, D. P. Tieleman, A. L. T. M. Sijbers, B. Hess, K. A. Feenstra, E. Lindahl, R. van Drunen, et al., *Gromacs User Manual version 3.1*, Nijenborgh 4, 9747 AG Groningen, The Netherlands. Internet: <http://www.gromacs.org> (2001).
 - [45] H. Flyvbjerg and H. G. Petersen, *J. Chem. Phys.* **91**, 461 (1989).
 - [46] H. J. C. Berendsen, J. P. M. Postma, W. F. van Gunsteren, A. DiNola, and J. R. Haak, *J. Chem. Phys.* **81**,

- 3684 (1984).
- [47] H. J. C. Berendsen, J. R. Grigera, and T. P. Straatsma, *J. Phys. Chem.* **91**, 6269 (1987).
 - [48] B. Guillot and Y. Guissani, *J. Chem. Phys.* **99**, 8075 (1993).
 - [49] M. W. Mahoney and W. L. Jorgensen, *J. Chem. Phys.* **112**, 8910 (2000).
 - [50] B. Widom, *J. Chem. Phys.* **39**, 2808 (1963).
 - [51] D. Frenkel and B. Smit, *Understanding Molecular Simulation — From Algorithms to Applications* (Academic Press, San Diego, 2002), 2nd ed.
 - [52] G. L. Deitrick, L. E. Scriven, and H. T. Davis, *J. Chem. Phys.* **90**, 2370 (1989).
 - [53] G. L. Deitrick, L. E. Scriven, and H. Davis, *Molecular Simulation* **8**, 239 (1992).
 - [54] M. Neumann, *Mol. Phys.* **50**, 841 (1983).
 - [55] J. E. Roberts and J. Schnitker, *J. Chem. Phys.* **101**, 5024 (1994).
 - [56] J. E. Roberts and J. Schnitker, *J. Phys. Chem.* **99**, 1322 (1995).
 - [57] S. R. Durell and A. Wallqvist, *Biophysical Journal* **71**, 1695 (1996).
 - [58] S. Boresch and O. Steinhauser, *J. Chem. Phys.* **115**, 10793 (2001).
 - [59] R. Fernandez-Prini and R. Crovetto, *J. Phys. Chem. Ref. Data* **18**, 1231 (1998).
 - [60] W. Wagner and A. Pruß, *J. Phys. Chem. Ref. Data* **31**, 387 (2002).
 - [61] A. Luzar and D. Chandler, *Nature* **379**, 55 (1996).
 - [62] A. Geiger, P. Mausbach, and J. Schnitker, in *Water and Aqueous Solutions*, edited by G. W. Neilson and J. E. Enderby (Adam Hilger, Bristol, 1986), pp. 15–30.
 - [63] F. Sciortino, A. Geiger, and H. E. Stanley, *Nature* **354**, 218 (1991).
 - [64] F. Sciortino, A. Geiger, and H. E. Stanley, *J. Chem. Phys.* **96**, 3857 (1992).
 - [65] P. H. Poole, F. Sciortino, U. Essmann, and H. E. Stanley, *Nature* **360**, 324 (1992).
 - [66] P. H. Poole, F. Sciortino, U. Essmann, and H. E. Stanley, *Phys. Rev. E* **48**, 3799 (1993).
 - [67] H. S. Ashbaugh, T. M. Truskett, and P. G. Debenedetti, *J. Chem. Phys.* **116**, 2907 (2002).
 - [68] F. W. Starr, J. K. Nielsen, and H. E. Stanley, *Phys. Rev. Lett.* **82**, 2294 (1999).